THE ASTROPHYSICAL JOURNAL, 414:357–371, 1993 September 1

THREE-DIMENSIONAL MAGNETOHYDRODYNAMICS OF THE EMERGING MAGNETIC FLUX IN THE SOLAR ATMOSPHERE

R. MATSUMOTO,[1,2] T. TAJIMA,[1] K. SHIBATA,[3] AND M. KAISIG[1,4]
Received 1992 November 5; accepted 1993 March 12

ABSTRACT

The nonlinear evolution of an emerging magnetic flux tube or sheet in the solar atmosphere is studied through three-dimensional (3D) magnetohydrodynamic simulations. In the initial state, a horizontal magnetic flux sheet or tube is assumed to be embedded at the bottom of magnetohydrostatic two isothermal gas layers, which approximate the solar photosphere/chromosphere and the corona. The magnetic flux sheet or tube is unstable against the undular mode of the magnetic buoyancy instability. The magnetic loop rises due to the linear and then later nonlinear instabilities caused by the buoyancy enhanced by precipitating the gas along magnetic field lines. We find by 3D simulation that during the ascendance of loops the bundle of flux tubes or even the flux sheet develops into dense gas filaments pinched between magnetic loops. The interchange modes help produce a fine fiber flux structure perpendicular to the magnetic field direction in the linear stage, while the undular modes determine the overall buoyant loop structure. The expansion of such a bundle of magnetic loops follows the self-similar behavior observed in 2D cases studied earlier. Our study finds the threshold flux for arch filament system (AFS) formation to be $\sim 0.3 \times 10^{20}$ Mx.

Subject headings: instabilities — MHD — Sun: atmosphere — Sun: magnetic fields

1. INTRODUCTION

The magnetic activity observed in the Sun originates from the emergence of magnetic flux created deep in the interior of the convection zone (e.g., Parker 1979). The newly emerged bipolar active regions are called emerging magnetic flux regions (EFRs; Zirin 1970, 1972).

In previous papers (Shibata et al. 1989a, b, 1990a; Shibata, Tajima, & Matsumoto 1990b; Kaisig et al. 1990; Nozawa et al. 1992), we studied the nonlinear evolution of emerging magnetic flux using a two-dimensional (2D) magnetohydrodynamic (MHD) code. In these 2D models, expanding magnetic loops are formed as a result of the nonlinear growth of the undular mode ($\boldsymbol{k} \parallel \boldsymbol{B}$ where $\boldsymbol{k}$ is the wavevector and $\boldsymbol{B}$ is the magnetic field vector) of the magnetic buoyancy instability (Fig. 1*c*) in a horizontal flux sheet embedded at the bottom of photosphere (Shibata et al. 1989a, b; Shibata et al. 1990b) or in the convection zone (Shibata et al. 1990a; Nozawa et al. 1992).

The undular mode grows for long-wavelength perturbations along the magnetic field lines, when the magnetic buoyancy created by gas sliding along a field line is greater than the restoring magnetic tension. The most unstable wavelength is $\sim 15H$, where H is the pressure scale height (e.g., Parker 1979). The undular instability is called the Parker instability in astrophysics because Parker (1966) applied this instability to the cloud formation in galactic gas disks.

In the nonlinear stage of the undular instability, Shibata et al. (1989a) found through 2D simulations that the expanding magnetic loops evolve self-similarly. Numerical results showed that the rising velocity of magnetic loops, V_z, is proportional to z until the top of the magnetic loop enters the corona. The density and magnetic field strength have power-law distributions $\rho \propto z^{-4}$ and $B_x \propto z^{-1}$, where z is the height measured from the base of the magnetic flux sheet. On the basis of these results, Shibata et al. (1990b) obtained an analytical self-similar solution which agrees well with the numerical results. The numerically obtained rise velocity of the magnetic loop in the high chromosphere is 10–15 km s^{-1}, and the velocity of downflow along the loop is 30–50 km s^{-1}, both of which are consistent with observed values for arch filament systems (AFS; Bruzek 1967, 1969; Chou & Zirin 1988).

The localized magnetic flux sheet under gravity can also be unstable against the interchange instability ($\boldsymbol{k} \perp \boldsymbol{B}$; Fig. 1*b*). Cattaneo & Hughes (1988) and Cattaneo, Chiueh, & Hughes (1990) performed nonlinear 2.5D simulations (2.5D means that we include the vector components in the third direction but ignore the variation in the third direction) of the interchange instability including the diffusive effects such as viscosity, resistivity, and thermal conductivity. We will show in §§ 3.4 and 3.5 of this paper the results of 2.5D ideal MHD simulation of the pure interchange mode (Fig. 1*b*) and mixed mode (Fig. 1*d*) of the magnetic buoyancy instability. In order to simulate the nonlinear growth of non–plane-wave perturbations (Fig. 1*e*), however, we need to perform full 3D simulations.

Recently, Matsumoto & Shibata (1992) carried out 3D-MHD simulations of the Parker instability in galactic gas disks and in EFRs. In this paper, we present a more detailed analysis of the 3D nonlinear simulations of emerging magnetic flux regions. The evolution of the emerging magnetic flux depends on the initial configuration of the magnetic flux and the initially stored magnetic energy. We consider two types of unperturbed magnetic field distributions; a horizontal magnetic flux sheet, and a horizontal magnetic flux tube. The expansion law of the magnetic loops are modified from those in 2D expansion because in three-dimensions the magnetic loops can expand perpendicularly to the field lines in two directions, vertically and horizontally.

[1] Institute for Fusion Studies, The University of Texas at Austin, Austin, TX 78712.
[2] College of Arts and Sciences, Chiba University, Inage-Ku, Chiba 263, Japan.
[3] National Astronomical Observatory, Mitaka, Tokyo 181, Japan.
[4] Institut für Astronomie und Astrophysik, Universität Würzburg, Am Hubland, 8700 Würzburg, Germany.

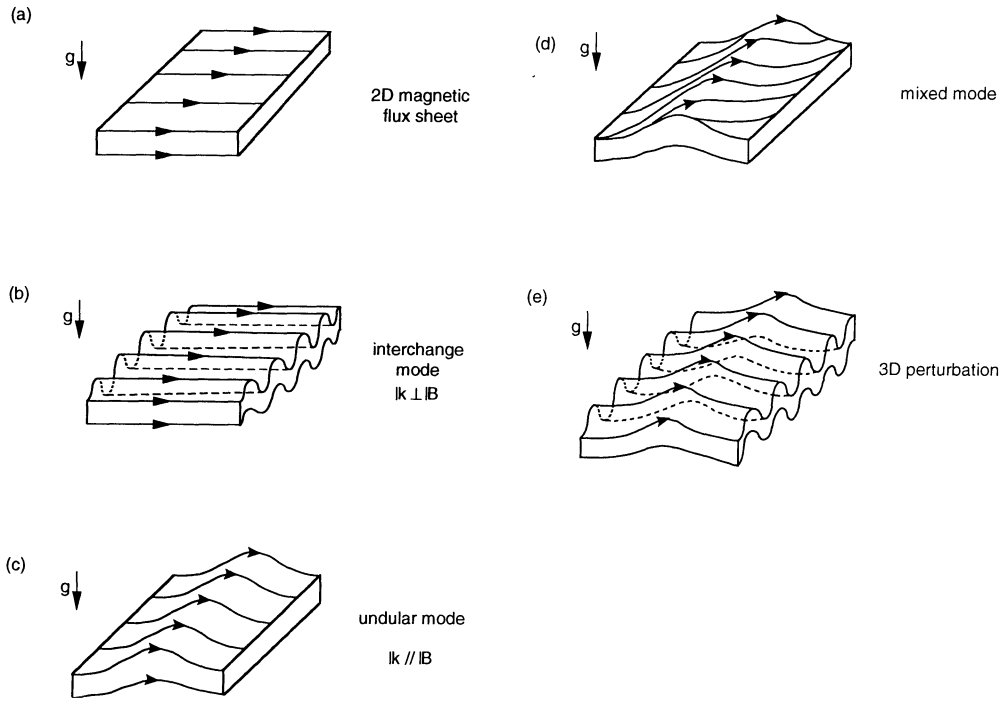

FIG. 1.—(*a–e*) A schematic picture of the magnetic buoyancy instability in a magnetic flux sheet

Section 2 gives assumptions, basic equations and numerical procedures. Numerical results are shown in § 3. In § 4, we discuss our results and summarize.

2. METHOD OF NUMERICAL SIMULATIONS

We assume that the medium is an ideal gas and the magnetic field is frozen in the gas. The gravitational acceleration, g, is assumed constant. Using the Cartesian coordinates (x, y, z), we take the z-direction antiparallel to the gravitational acceleration vector. The basic equations are

$$\frac{\partial \rho}{\partial t} + \nabla \cdot (\rho \boldsymbol{V}) = 0 , \tag{1}$$

$$\frac{\partial (\rho \boldsymbol{V})}{\partial t} + \nabla \cdot \left(\rho \boldsymbol{V}\boldsymbol{V} + p\boldsymbol{I} - \frac{\boldsymbol{B}\boldsymbol{B}}{4\pi} + \frac{\boldsymbol{B}^2}{8\pi}\boldsymbol{I} \right) - \rho \boldsymbol{g} = 0 , \tag{2}$$

$$\frac{\partial \boldsymbol{B}}{\partial t} = \nabla \times (\boldsymbol{V} \times \boldsymbol{B}) , \tag{3}$$

$$\frac{\partial}{\partial t}\left(\rho U + \frac{1}{2}\rho V^2 + \frac{\boldsymbol{B}^2}{8\pi} \right) + \nabla \cdot \left[\left(\rho U + p + \frac{1}{2}\rho V^2 \right) \boldsymbol{V} + \frac{c}{4\pi} \boldsymbol{E} \times \boldsymbol{B} \right] - \rho \boldsymbol{g} \cdot \boldsymbol{V} = 0 , \tag{4}$$

$$U = \frac{1}{\gamma - 1}\frac{p}{\rho} , \tag{5}$$

$$\boldsymbol{E} = -\frac{1}{c}\boldsymbol{V} \times \boldsymbol{B} , \tag{6}$$

where U is the internal energy per unit mass, $\boldsymbol{I}$ is the unit tensor, $\boldsymbol{g} = (0, 0, -g)$ is the gravitational acceleration, γ is the specific heat ratio, and the other symbols have their usual meanings.

The unperturbed state is a two isothermal gas layer which we take as a very simplified model of the solar corona and chromosphere/photosphere. The initial temperature distribution outside the magnetic flux tube has the assumed form

$$T(z) = T_{\rm ch} + (T_{\rm cor} - T_{\rm ch})\frac{1}{2}\left[\tanh\left(\frac{z - z_{\rm cor}}{w_{tr}} \right) + 1 \right] , \tag{7}$$

where $T_{\rm cor}/T_{\rm ch}$ (= 25 for all our calculations) is the ratio of the temperature in the corona to that in the chromosphere/photosphere, $z_{\rm cor}$ is the height of the base of the corona, and w_{tr} is the temperature scale height in the transition region (= $0.6H$ for all our models).

We assume that the magnetic field is initially parallel to the x-direction and is localized in the photosphere with the distribution

$$B_x(y, z) = [8\pi p(y, z)/\beta(y, z)]^{1/2} , \tag{8}$$

where $\beta(y, z)$ is the local plasma β assumed to be

$$\beta(y, z) = \beta_0 / f(y, z) , \tag{9}$$

$$f(y, z) = \frac{1}{16}\left[\tanh\left(\frac{z - z_0}{w_0} \right) + 1 \right]\left[-\tanh\left(\frac{z - z_1}{w_1} \right) + 1 \right] \times \left[\tanh\left(\frac{y - y_0}{w_y} \right) + 1 \right]\left[-\tanh\left(\frac{y - y_1}{w_y} \right) + 1 \right] . \tag{10}$$

Here β_0 is the ratio of gas pressure to magnetic pressure at the center of the magnetic flux tube, z_0 and $z_1 = z_0 + D$ are the heights of the lower and upper boundaries of the magnetic flux tube, respectively. The horizontal width of the magnetic flux tube is $W = y_1 - y_0$. The initial density and pressure distributions come from numerically solving the equations of static

pressure balance

$$\frac{d}{dz}\left[p + \frac{B_x(y, z)^2}{8\pi}\right] + \rho g = 0 . \quad (11)$$

In magnetic flux sheet models, we assume $y_0 = -\infty$ and $y_1 = \infty$. In all models described in this paper, we adopt $z_0 = 0$, $D = 4H$, and $w_0 = w_1 = w_y = 0.5H$. In the magnetic tube models, we assume that the density inside the tube is the same as that outside the tube at the same height.

We impose symmetric boundaries at $x = 0$ and $x = X_{max}$, periodic boundaries at $y = 0$ and $y = Y_{max}$, a symmetric (rigid conducting wall) boundary at $z = Z_{min} = -4H$, and a free boundary at $z = Z_{max}$. The effect of the free boundary at $z = Z_{max}$ is minimal.

To start the dynamical evolution, we impose initial perturbations on the magnetic flux sheet or tube. In localized perturbation models, the small velocity perturbations have the form

$$V_x = f(y, z)AC_s \sin\left[\frac{2\pi(x - X_{max})}{\lambda_x}\right] \cos\left(\frac{2\pi y}{\lambda_y}\right) \quad (12)$$

within the finite horizontal domain $(X_{max} - \lambda_x/2 \le x \le X_{max})$, where λ_x and λ_y are the wavelength of the small velocity perturbation in the x- and y-directions, respectively, C_s is the sound speed in the low-temperature layer, and A is the maximum value of V_x/C_s in the initial perturbation. The wavenumbers of the perturbation in x- and y-directions are k_x ($= 2\pi/\lambda_x$) and k_y ($= 2\pi/\lambda_y$), respectively.

Equations (1)–(4) are rendered dimensionless by using the normalizing constants H, C_s, and ρ_0, where ρ_0 is the density at the base of the gas layer ($z = -4H$). The unit of time is $\tau = H/C_s$. When we compare numerical results with observations, we use $H = 200$ km, $C_s = 10$ km s^{-1}, and $\tau = 20$ s, which are typical values for the solar chromosphere and photosphere.

Equations (1)–(4) are solved numerically by a modified Lax-Wendroff scheme (Rubin & Burstein 1967), with artificial viscosity (Richtmyer & Morton 1967). The accuracy of such a MHD code is described in Shibata (1983), Shibata & Uchida (1985), Matsumoto et al. (1988), and Umemura et al. (1988). The grid spacing is uniform in x- and y-directions, but slowly increasing with z in the corona.

Here we shall comment on the effects of the diffusion terms (viscosity, resistivity, and thermal conduction) ignored in our basic equations (1)–(4). In the convectively stable region where the buoyancy frequency $N^2 = (g/\gamma)d\ln(P\rho^{-\gamma})/dz > 0$, the ordinary buoyancy force becomes a restoring force, which has the stabilizing effect on the magnetic buoyancy instability. According to the linear stability analysis including diffusive terms (e.g., Acheson 1979), the stabilizing effect is reduced by a factor η/κ, where η and κ are the magnetic diffusivity, and the thermal diffusivity, respectively. In the solar interior where $\kappa \gg \eta$, this "double diffusive" reduction of stratification effects makes the magnetic buoyancy instability more easy to take place than in adiabatic gas layers. As in thermosolutal convection, which is a typical example of double diffusive system, the diffusion terms can also drive overstable oscillations of flux sheets around their equilibrium position (Acheson 1979; Hughes 1985). The viscous term helps stabilizing the magnetic buoyancy instability, especially for short wavelength modes perpendicular to the field lines (Acheson 1979).

The models examined in this paper appear in Table 1. In all models, by using an adiabatic index $\gamma = 1.05$, we reduced the stabilizing effect of the normal buoyancy force compared to the case with $\gamma = 5/3$. Note, however, that the flux tubes in models 9 and 10 will become more buoyant if the effects of thermal diffusion is included, because the flux tubes in the initial state are cooler than the surrounding non-magnetic gas in order for such flux tubes to be in static equilibrium with surroundings.

Although we solve the ideal MHD equations, we cannot avoid numerical diffusion. We confirmed that when no perturbation is imposed, the initial equilibrium state is unchanged over the time scale of simulation reported in this paper ($\sim 100H/C_s$). The effect of numerical diffusion is minimal for waves whose wavelength is longer than 10 grid points. The artificial viscosity has no effect in smooth region because it is switched on only in the region with steep velocity gradient such as shock waves.

3. RESULTS

3.1. *Nonlinear Evolution of the Three-dimensional Magnetic Buoyancy Instability in an Isolated Horizontal Flux Sheet*

Figure 2 shows the time evolution of the 3D magnetic buoyancy instability for a typical model (model 1), where the model parameters are $\beta_0 = 1$, $\gamma = 1.05$, $z_{cor} = 14H$, $W = \infty$, $\lambda_x = \lambda_y = 20H$, and $A = 0.05$. The model volume is $L_x \times L_y \times L_z = 40H \times 20H \times 35H$, and the number of grid points is $N_x \times N_y \times N_z = 43 \times 42 \times 101$. The solid curves show isocontours of the vector potential A_y in $y = 0$ plane, which approximate the magnetic field lines if the field configuration is roughly two-dimensional. By using the symmetric condition at $x = 40H$, twice the computing area is shown in the figure. As the instability grows, the magnetic flux rises buoyantly as the

TABLE 1

MODELS EXAMINED IN THIS PAPER

Model	β_0	W/H	λ_x/H	λ_y/H	A	Volume $(L_x L_y L_z/H^3)$	Grid $(N_x N_y N_z)$
1.....	1.0	∞	20	20	0.05	40 × 20 × 35	43 × 42 × 101
2.....	1.0	∞	20	∞	0.05	40 × 24.5	53 × 82
3.....	1.0	∞	20	38.4	0.05	40 × 38.4 × 24.5	53 × 51 × 82
4.....	1.0	∞	20	4.8	0.05	40 × 4.8 × 24.5	53 × 51 × 82
5.....	0.2	∞	...	10	0.01	40 × 35	101 × 172
6.....	1.0	∞	...	Random	0.01	40 × 35	162 × 101
7.....	1.0	∞	20	...	0.05	80 × 35	101 × 172
8.....	1.0	∞	Random	Random	0.01	80 × 20 × 35	42 × 42 × 101
9.....	1.0	4.0	20	...	0.05	40 × 40 × 28	43 × 18 × 92
10.....	1.0	4.0	20	...	0.05	40 × 12 × 28	43 × 18 × 92

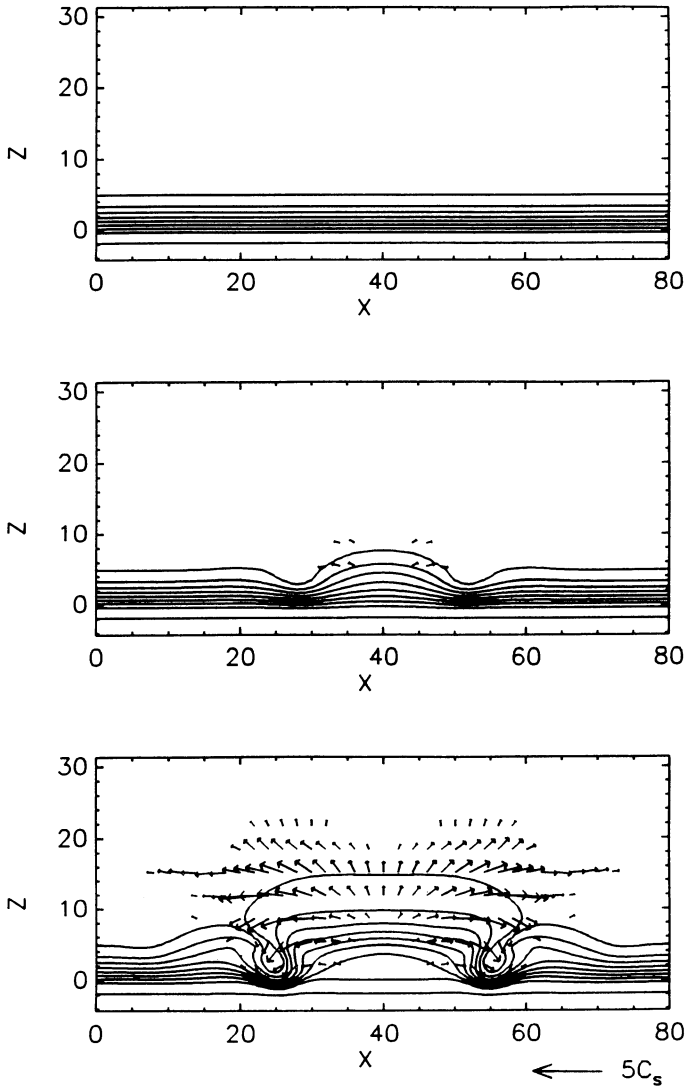

FIG. 2.—Evolution of the magnetic buoyancy instability in model 1 ($\beta_0 = 1$, $\lambda_x = \lambda_y = 20H$) at $y = 0$ plane. The solid curves are isocontours of the vector potential, A_y, which approximately show magnetic field lines. The arrows show velocity vectors. The unit of the velocity vectors is shown at the right bottom. *Top*: $t/\tau = 0.0$. *Middle*: $t/\tau = 24.2$ *Bottom*: $t/\tau = 36.9$.

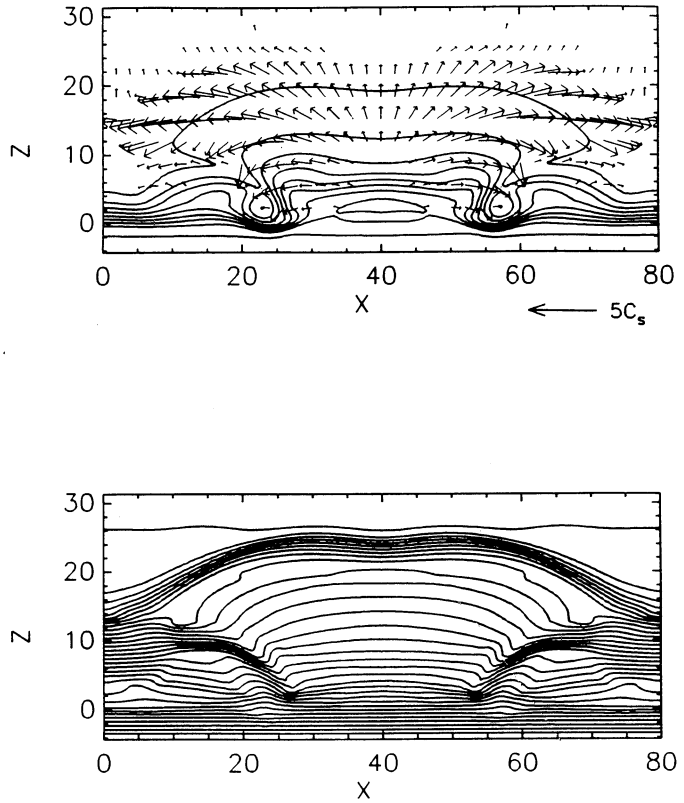

FIG. 3.—Nonlinear stage of the magnetic buoyancy instability ($t = 41.9H/C_s$) in model 1 at $y = 0$ plane. The upper panel shows the isocontour curves of the magnetic vector potential A_y (*solid curves*), and velocity fields (*arrows*). The unit of the velocity vectors is shown at the right bottom. The lower panel shows the isodensity curves. The interval of the isocontours is 0.25 in logarithmic scale.

gas slides down along the forming loop and matter accumulates in a magnetic pocket at the base of the loop.

Figure 3 shows isocontours of A_y, velocity vectors (upper panel), and log ρ (lower panel) in $y = 0$ plane at $t = 41.9\tau$. Notice the approximately self-similar expansion of the magnetic loops, and the shock wave formation at the footpoints of the magnetic loops, both of which also appeared in the nonlinear stage of the two-dimensional magnetic flux expansion (Shibata et al. 1989a, b; Shibata et al. 1990b). Strong MHD shock waves are formed at the footpoints of the loop, because the maximum downflow speed is about $4C_s - 5C_s$, which exceeds both the local sound speed and the Alfvén speed ($V_A \simeq 2C_s - 3C_s$). We can identify a fast MHD shock in the lower region and an intermediate MHD shock in the upper region, although the structure of these shocks is not as clear as in the 2D simulations (Shibata et al. 1989b) because of coarser grids in 3D simulation.

To bring out the three-dimensional structure, we show in Figure 4 the magnetic field configuration, velocity field, and the density distribution in the $y = 10H$ plane. Interleaved structure of magnetic field lines is created by the growth of the imposed velocity perturbation (eqn. [12]), which has the opposite direction in the $y = 0$ plane (Fig. 3) and $y = 10H$ plane (Fig. 4).

To see the interleaved structure better, we show a perspective view of some magnetic field lines and their projection onto the $y - z$ plane in Figure 5. Thick curves show magnetic field lines which start from $(x, y, z) = (0, H, 3.5H)$ and $(x, y, z) = (0, 19H, 3.5H)$. They are pushed toward $y = 10H$ around $x = 40H$ by horizontal expansion. Figure 6 shows the distribution of density, velocity field, and B_x in the $z = 13.5H$ plane at $t = 36.9\tau$. A dense filament is formed between expanding magnetic loops, where the gas in the flux tubes adjacent in the y-direction is compressed by the horizontally expanding motion of the magnetic loops. The computationally observed filamentary distribution of dense gas is a common feature in the nonlinear stage of 3D magnetic buoyancy instability (Matsumoto & Shibata 1992). Such filaments may correspond to the arch filaments observed in emerging flux regions of the Sun (Bruzek 1967). The length of the filament is $30H \simeq 6000$ km, and the width is $4H \simeq 800$ km.

The density distribution in the $x = 40H$ plane in Figure 7*a* also shows the density enhancement around $y = 10H$ and

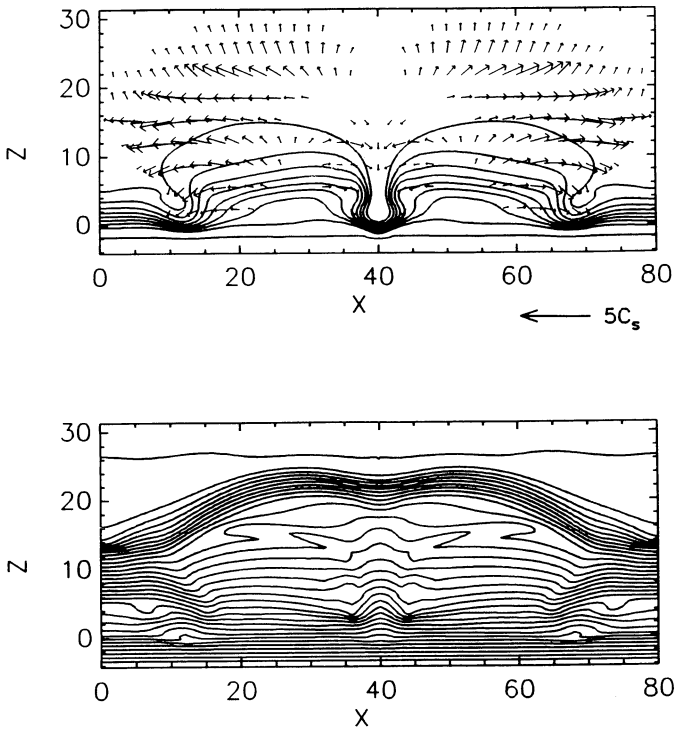

FIG. 4.—The same as in Fig. 3 but at $y = 10.0H$

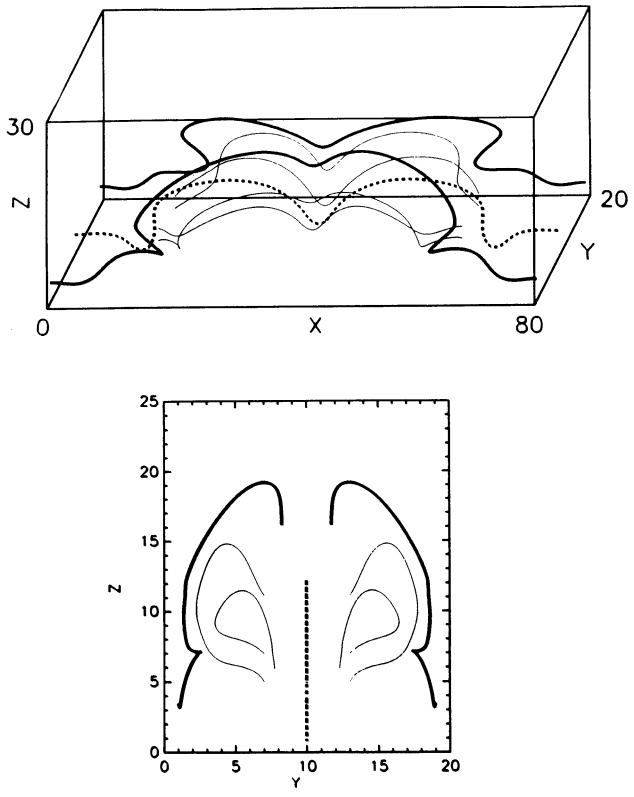

FIG. 5.—Three-dimensional structure of some magnetic field lines in model 1 at $t = 41.9H/C_s$ (*top*) and their projection onto the $y - z$ plane (*bottom*). Thick curves show magnetic field lines starting from $(x, y, z) = (0, H, 3.5H)$ and $(x, y, z) = (0, 19H, 3.5H)$. Dashed curve shows a magnetic field line starting from $(x, y, z) = (0, 10H, 3.5H)$. Thin curves show examples of twisted magnetic field lines.

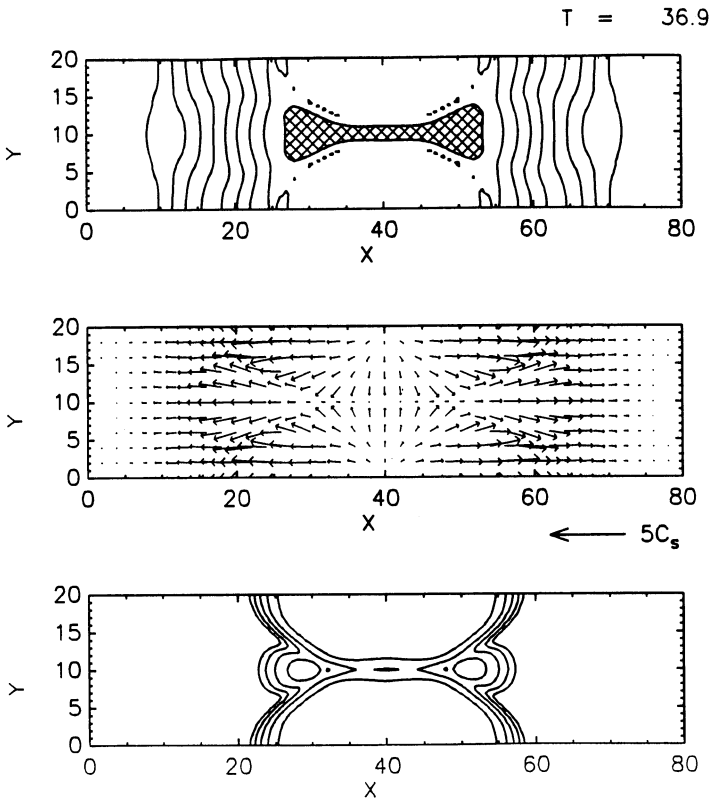

FIG. 6.—The distribution of density, velocity field, and horizontal magnetic field (B_x) in the nonlinear stage ($t = 36.9H/C_s$) of model 1. The slices at $z = 13.5H$ are shown. The step width of the density isocontours is 0.25 in logarithmic scale. The dense region is indicated by hatch.

$z = 13H$. The rising speed of the filament is $1\text{–}1.5C_s \simeq 10\text{–}15$ km s^{-1}. As seen in Figure 7*b*, the horizontal expansion of the rising flux tubes produces a vortex motion. This then twists the magnetic fields and generates torsional Alfvén waves. Examples of field lines twisted by the vortex motion appear in Figure 5 as thin curves.

3.2. *Quasi–self-similar Expansion of Magnetic Loops*

Time evolution of the rise velocity, mass density, local Alfvén speed, and B_x at the midpoint of the loop are shown in Figure 8 for model 1. We find approximately self-similar evolution of magnetic loops. The dashed curves in Figure 8 correspond to a particular self-similar solution ($\rho \propto z^{-4}$, $B_x \propto z^{-1}$) previously found for 2D loops (Shibata et al. 1989a; Shibata, Tajima, & Matsumoto 1990b). The 3D numerical results can also be fitted to these solutions, although B_x decreases faster than z^{-1}, and $V_A = B_x/\sqrt{4\pi\rho} \simeq$ const in the early stage of evolution or around the top of magnetic loops.

The physical meaning of the self-similar solution becomes clear by considering the phenomenological equation of motion near the midpoint of the loop (Shibata et al. 1990b),

$$\frac{\partial V_z}{\partial t} = -g - \frac{1}{\rho}\frac{\partial p}{\partial z} - \frac{1}{\rho}\left[\frac{\partial}{\partial z}\left(\frac{B_x^2}{8\pi}\right) + \frac{B_x^2}{4\pi R}\right], \qquad (13)$$

where R is the curvature radius of the loop. In the region where $\rho \propto z^{-4}$ and $B_x \propto z^{-1}$, the third term (magnetic pressure term) in the right-hand side of equation (13) dominates over gravity,

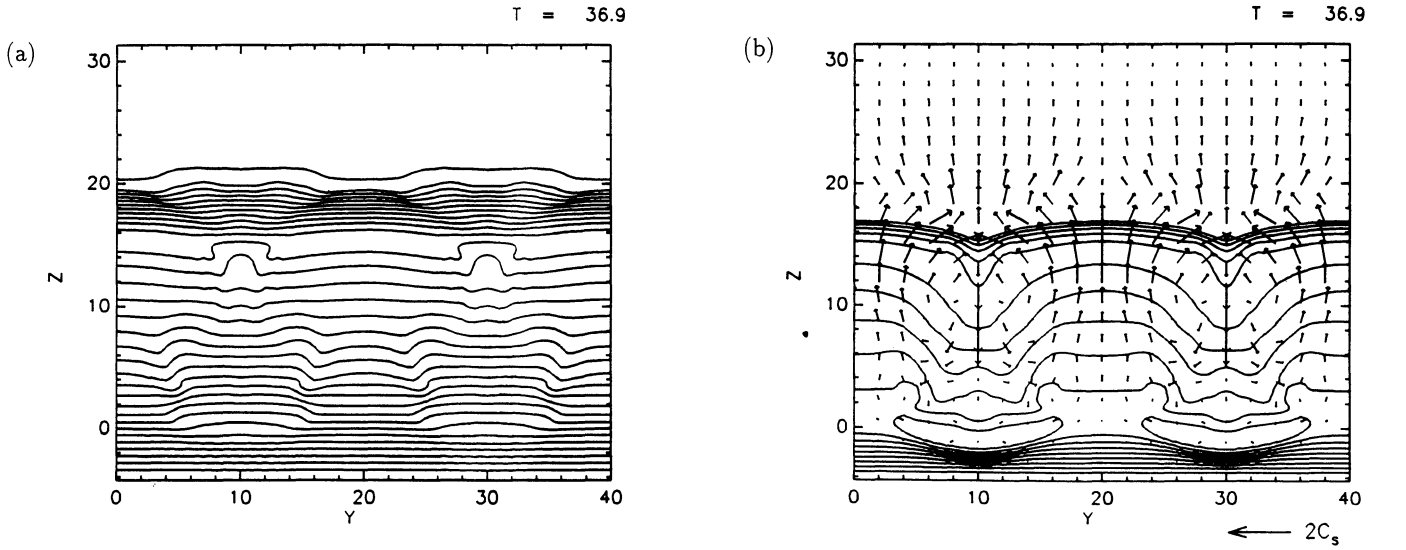

FIG. 7.—(*a*) The density distribution, and (*b*) isocontours of magnetic field strength (B_x), and the velocity field in model 1 at $t = 36.9H/C_s$. The slices at $x = 40H$ are shown. The unit of velocity vectors is shown at the right bottom of the figures. The step width of the density isocontours is 0.25 in logarithmic scale.

the pressure gradient force, and the magnetic tension, and balances with the left-hand side which scales as $z \propto \exp(at)$ in the exponentially expanding stage (Shibata et al. 1990b).

From flux conservation, the $B_x \propto z^{-1}$ dependence indicates that the cross-sectional area of the magnetic loop is expanding quasi one-dimensionally in the z-direction. This regime appears after the expanding magnetic loop interacts with the adjacent loop (see e.g., Fig. 6). Since the horizontal expansion of the magnetic loop is limited by the adjacent loop, the loop expansion can occur only in the z-direction. On the other hand, the magnetic field can expand both in the y- and z-directions in the early stage of the nonlinear evolution or around the top of emerging loops; then, in these cases B_x decreases faster than z^{-1}. The $\rho \propto z^{-4}$ dependence comes from

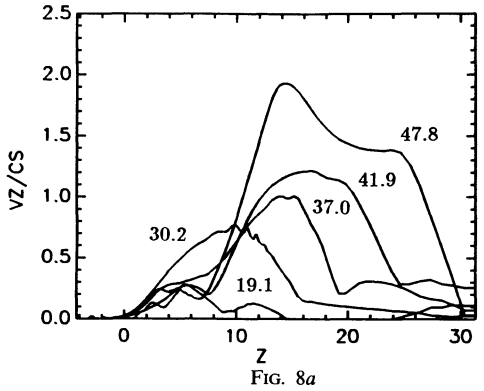

FIG. 8*a*

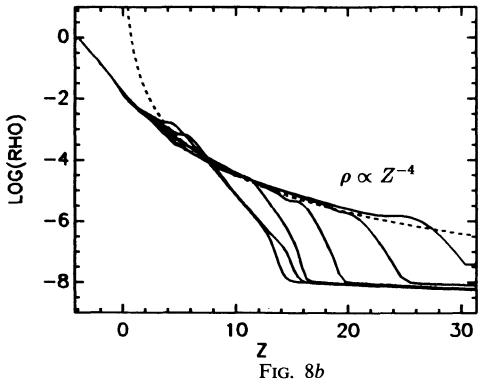

FIG. 8*b*

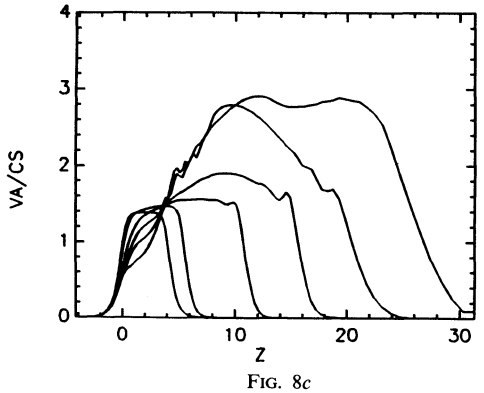

FIG. 8*c*

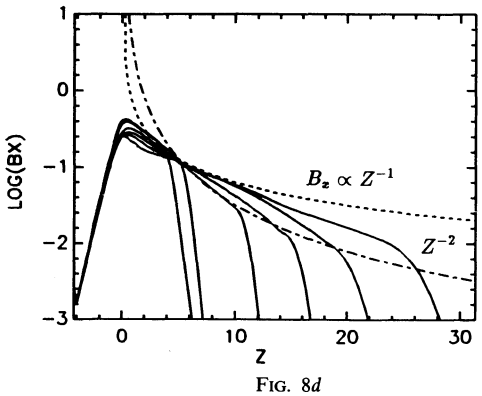

FIG. 8*d*

FIG. 8.—The distribution of the (*a*) rising speed V_z, (*b*) density ρ, (*c*) Alfvén speed V_A, and (*d*) the horizontal magnetic field B_x for model 1 at the midpoint of the loop ($x = 40H$, $y = 0$). Each solid curve corresponds to $t/\tau = 0$, 19.1, 30.2, 37.0, 41.9, and 47.8, from left to right, respectively. The dashed curves denote the dependence z^{-4} for the density and z^{-1} for B_x. The dash-dotted curve denotes the dependence z^{-2}.

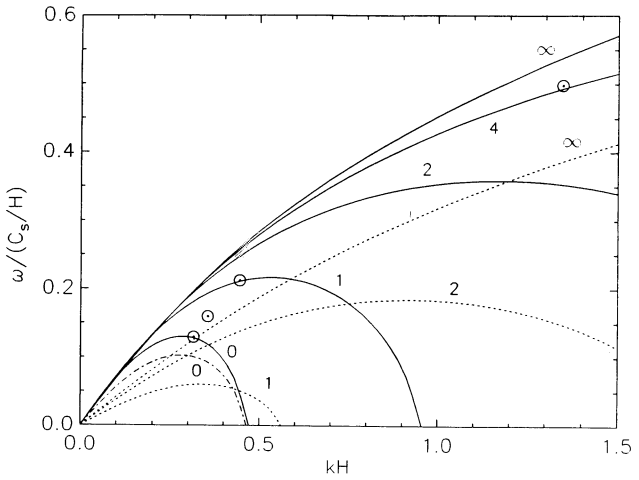

FIG. 9.—Linear growth rates of the magnetic buoyancy instability. The wavenumber k is defined as $k = (k_x^2 + k_y^2)^{1/2}$. Solid curves denote the growth rate of the magnetic buoyancy instability in magnetic flux sheet with $\gamma = 1.05$. See text for other parameters of the unperturbed flux sheet. The numbers attached to each curve denote the value of k_y/k_x. The dashed curves are for magnetic flux sheet with $\gamma = 5/3$. The dash-dotted curve is for a flux sheet with $\gamma = 1.05$ which has the same density distribution as the flux tube model adopted in this paper. Symbols denote the linear growth rate for model 2 ($k_x = 0.314$, $k_y = 0$), model 3 ($k_x = 0.314$, $k_y = 0.164$), model 1 ($k_x = 0.314$, $k_y = 0.314$), and model 4 ($k_x = 0.314$, $k_y = 1.309$) from bottom to top, respectively.

the evacuation of the magnetic loop by gravity (Shibata et al. 1990b).

3.3. *Dependence on the Wavelength of Perturbation Perpendicular to the Magnetic Field Lines*

Solid curves in Figure 9 show linear growth rates ω of the magnetic buoyancy instability in an isolated flux sheet with $\beta_0 = 1$, $\gamma = 1.05$, $D = 4H$, $Z_{cor} = 14H$ and $T_{cor}/T_{ch} = 25$ as a function of the horizontal wavenumber $k = (k_x^2 + k_y^2)^{1/2}$ (see Horiuchi et al. 1988 and Shibata et al. 1989a for details of the linear stability analysis). The numbers attached to each curve denote the ratio k_y/k_x. When the wavenumber along the field line (k_x) is fixed, the growth rate increases with the perpendicular wavenumber k_y. Thus a perturbation with a shorter wavelength perpendicular to the field line grows faster than long-wavelength perturbations. The dashed curves in Figure 9 show growth rates when $\gamma = 5/3$. Although we assumed $\gamma = 1.05$ for all our models in this paper, a gas with $\gamma = 5/3$ also becomes unstable against magnetic buoyancy instability for short-wavelength ($k_y > k_x$) perturbations perpendicular to the field lines. The dash-dotted curve in Figure 9 shows linear growth rates of the magnetic buoyancy instability in a flux sheet which has the same density distribution as in our flux tube model.

The linear growth rate of our nonsinusoidal perturbations (eqn. [12]) is the same as that in the mixed mode because this perturbation can be decomposed into two plane wave perturbations whose wave vectors are (k_x, k_y) and $(k_x, -k_y)$.

The time evolution of the rise velocity at the midpoint of the magnetic loop ($x = 40H$, $y = 0$) is shown in Figure 10 for several models. The model parameters are $Z_{cor} = 14H$, $A = 0.05$, and (*a*) $\lambda_y = \infty$ (model 2), (*b*) $\lambda_y = 38.4H$ (model 3), and (*c*) $\lambda_y = 4.8H$ (model 4). Other parameters are the same as in model 1. When the top of the magnetic loop is below the base altitude of the corona, the rise velocity of the magnetic loop increases linearly with height. This expansion law is written as

$$V_z/C_s = az/H \, . \tag{14}$$

The approximate values of a obtained from Figures 8 and 10 are 0.12, 0.08, 0.11, and 0.33, for models 1, 2, 3, and 4, respectively. These values are close to half of the linear growth rate of the magnetic buoyancy instability shown in Figure 9.

3.4. *Nonlinear Evolution of the Pure Interchange Mode*

The evacuation of matter at the top of the loop plays an essential role in forming rising magnetic loops in the Parker instability. On the other hand, the gas precipitation along the field lines during the buoyant motion is not allowed for the interchange instability. In order to show the difference between the undular mode and the interchange mode, we carried out 2.5D simulation of the pure interchange mode ($k_x = 0$), where the sliding motion of the gas along the field is forbidden.

Figure 11 shows a result of 2.5D simulation of the pure interchange mode (model 5). In this model, the initial velocity perturbation is imposed on V_z. The formation of a mushroom shaped interface between the magnetic field and field free gas, and the vortex motion are similar to the result of 2.5D simulation of pure interchange instability by Cattaneo & Hughes

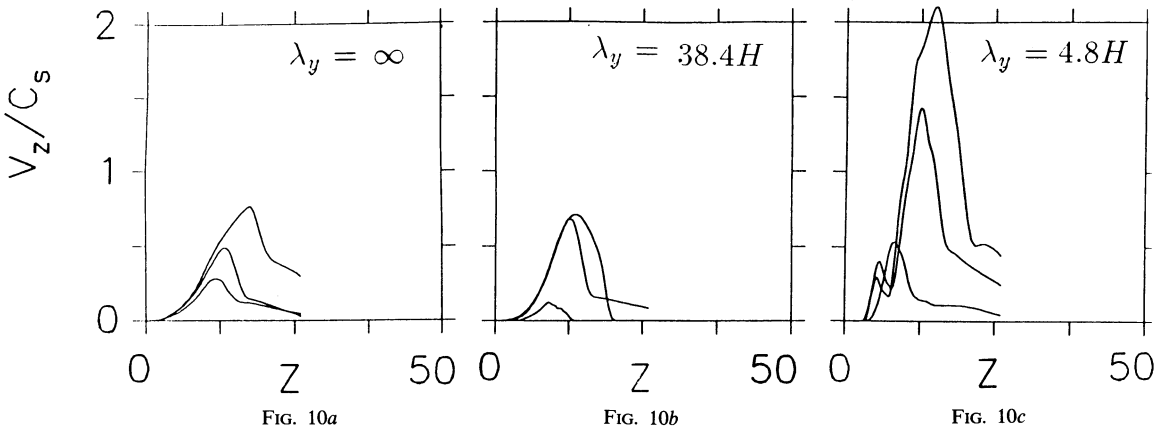

FIG. 10*a* FIG. 10*b* FIG. 10*c*

FIG. 10.—The evolution of the rising speed of the magnetic flux at the midpoint of the loop ($x = 40H$, $y = 0$) for (*a*) model 2 ($\lambda_y = \infty$), (*b*) model 3 ($\lambda_y = 38.4H$), and (*c*) model 4 ($\lambda_y = 4.8H$), respectively. The solid curves show the rising speed at (*a*) $t/\tau = 23.8$, 29.4, 34.8, (*b*) 12.0, 23.4, 31.8, and (*c*) 12.5, 21.5, 25.0, respectively, from bottom to top.

(1988), although the diffusion terms included in their simulation are absent in our model, and the thickness of the magnetic layer in our model is 5 times larger than theirs.

The rise velocity of the magnetic field saturates in a short time when it reaches the Alfvén speed evaluated at the initial conditions, and the vertical expansion is nearly halted at $t = 24.2\tau$. The deceleration of the rising motion can be explained by using equation (13). Since the cross-sectional area of the loop approximately scales as z^2, the density and horizontal magnetic field scale as z^{-2}. Thus the magnetic pressure gradient term in equation (13) decreases as z^{-3} and cannot drive the loop expansion in the nonlinear stage. From $\rho \propto z^{-2}$ and $B_x \propto z^{-2}$, we obtain $V_A \propto B_x/\rho^{1/2} \propto z^{-1}$. This dependence on z is consistent with the numerical result shown in Figure 12.

Figure 13 shows a result of 2.5D MHD simulation of the pure interchange instability when the random perturbations in V_z are imposed at the initial stage (model 6). The maximum amplitude of the velocity perturbation is $0.01C_s$.

At $t = 20.0\tau$, we find small ripples around the upper surface of the flux sheet. In ideal MHD, the growth rate of the pure

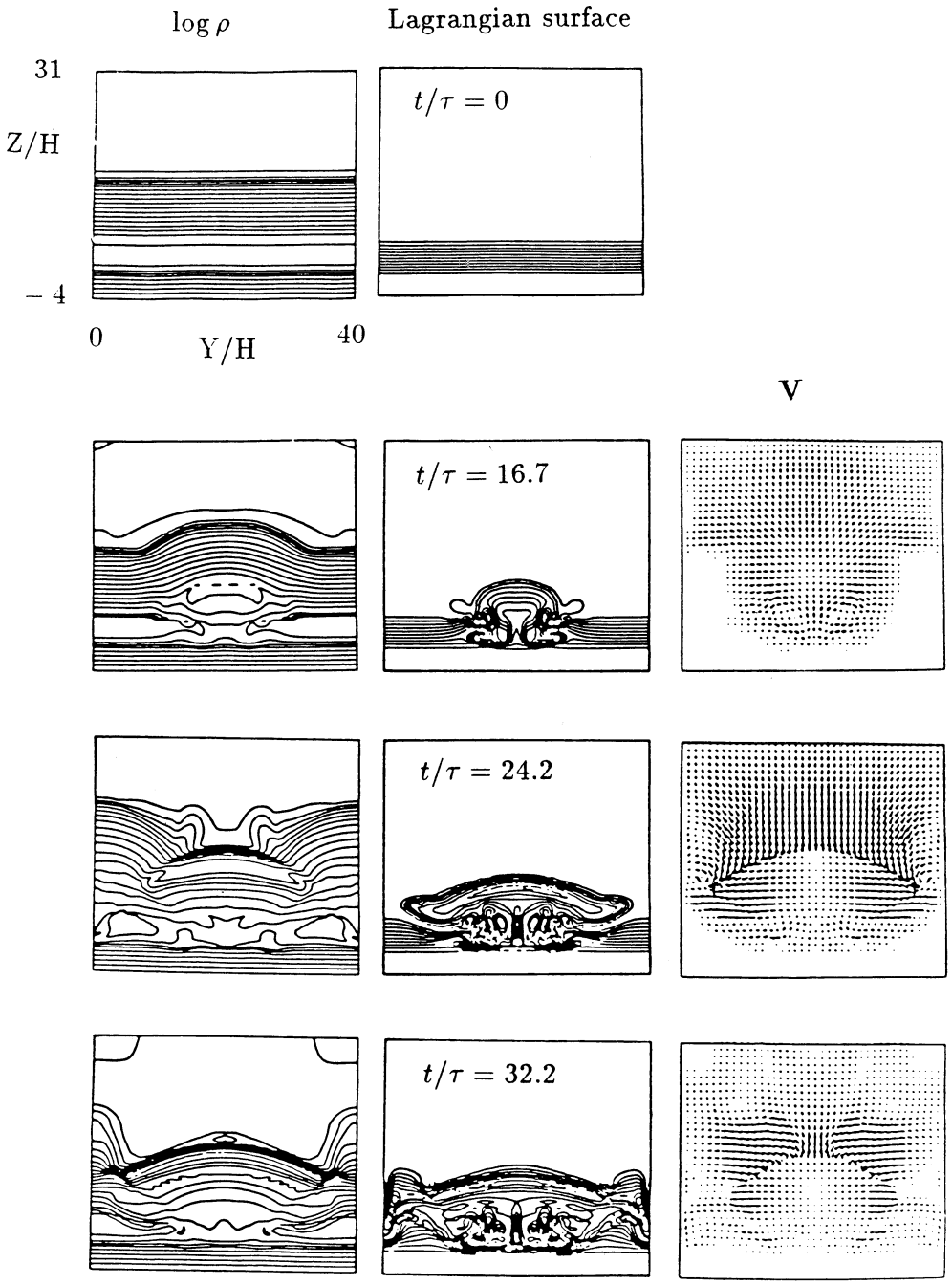

FIG. 11.—Evolution of the pure interchange mode for model 5 ($\beta_0 = 0.2$, $\lambda_y = 10H$). Left panels show the isocontours of density, midpanels show B_x, which trace the lagrangian position of each test particles, and the right panel shows the velocity distribution. The interval of the density isocontours is 0.25 in logarithmic scale.

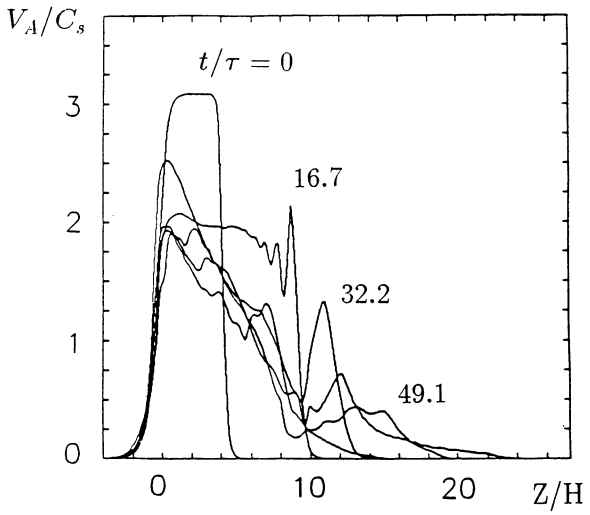

FIG. 12.—Evolution of the Alfvén speed at $y = 20H$ for model 5. Numbers attached to each curve denote time in unit of H/C_s.

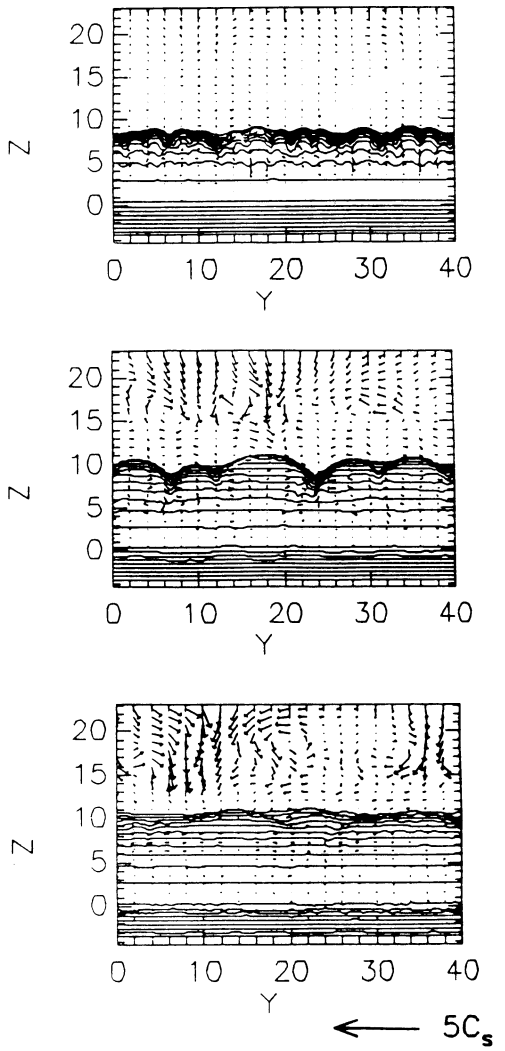

FIG. 13.—Evolution of the pure interchange mode when the random perturbation is imposed at the initial stage (model 6). The solid curves denote the isocontours of the strength of B_x. *Top*: $t/\tau = 20.0$. *Middle*: $t/\tau = 36.4$. *Bottom*: $t/\tau = 79.0$.

interchange mode is larger for shorter wavelength perturbation perpendicular to the magnetic field lines. In numerical simulation, however, waves with wavelength shorter than several times of the grid size are significantly dumped by numerical diffusion. This is the reason why pure interchange modes with wavelength 9–10 grid sizes grow fastest in the linear stage of our simulation. In the nonlinear stage, isolated flux tubes are not formed because horizontal expansion forces the flux tubes to merge. The vertical expansion speed decreases with time in the nonlinear stage.

Thus we conclude that nonlinear instability does not exist in the pure interchange instability and that the pure interchange instability alone cannot create emerging magnetic loops. These conclusions are in some part dependent on the absence of resistivity in our model. As we shall discuss in the next subsection, when the system evolves into a configuration suitable for magnetic reconnection, there is a possibility that isolated flux tubes are created by magnetic reconnection.

3.5. *Two-dimensional Mixed Mode*

The perturbations (eqn. [12]) imposed on the unperturbed flux sheet can be decomposed into two plane-wave perturbations which have the same linear growth rate. Here we present the results of nonlinear growth of one such mixed mode plane-wave perturbation.

Figure 14 shows the nonlinear stage of the mixed mode instability (model 7). In this model, the unperturbed magnetic fields have B_x and B_y components where $B_y(z)/B_x(z) = 1$; there is no magnetic shear. The imposed velocity perturbation has the form $V_x = AC_s \sin [2\pi(x - X_{max}/2)/\lambda_x]$ within the finite horizontal region $(X_{max}/2 - \lambda_x/2 \leq x \leq X_{max}/2 + \lambda_x/2)$ of magnetic sheet $(z_0 \leq z \leq z_1)$, where $A = 0.05$, $X_{max} = 80H$, and $\lambda_x = 20H$. The other parameters are the same as in model 1. We use a 2.5D MHD code to perform the numerical computation, with a periodic boundary condition assumed at $x = 0$ and $x = X_{max}$.

The nonlinear expansion of magnetic flux in the mixed mode is essentially the same as that found in the pure undular mode (Shibata et al. 1989a) and that in the 3D expansion (model 1). The rise velocity increases linearly with height and the expanding magnetic loop shows self-similar behavior.

The nonlinear growth of the mixed mode instability and its dependence on the thickness of the magnetic layer has been studied by S. Nozawa et al. (private communication) using 2.5D resistive MHD code. They found that when the thickness of the magnetic layer is smaller than the scale height, twisted flux tubes are formed in the nonlinear stage owing to the mag-

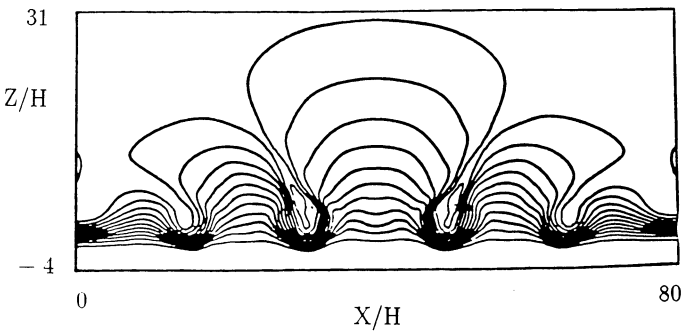

FIG. 14.—Nonlinear stage of the mixed mode instability for model 7 ($\beta_0 = 1$, $\lambda_x = 20H$). The solid curves denote the magnetic field lines. $t/\tau = 68.7$.

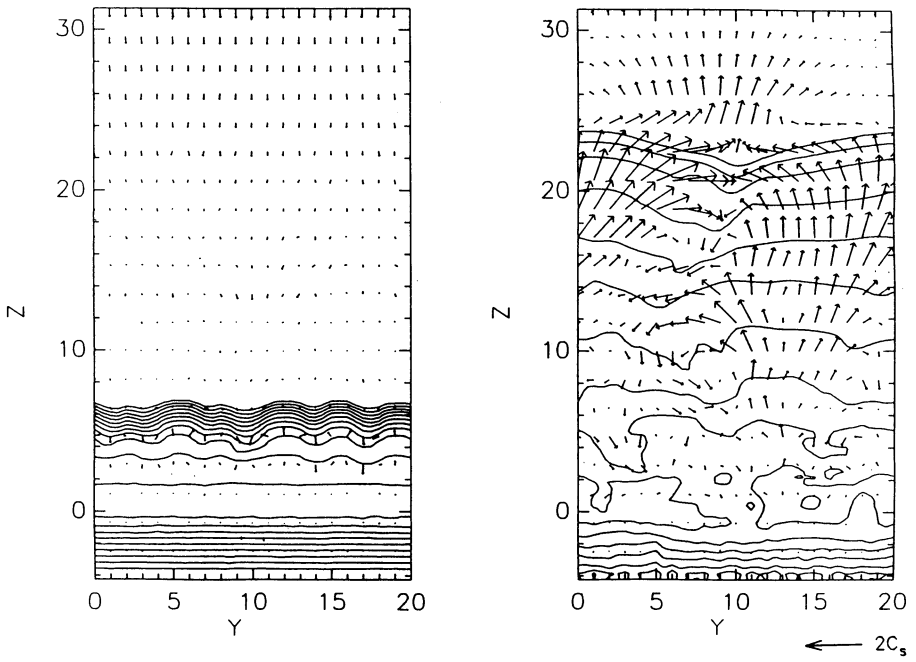

FIG. 15*a* FIG. 15*b*

FIG. 15.—Evolution of the magnetic buoyancy instability when the random perturbations are imposed in the magnetic flux sheet (model 8). The isocontours of B_x (*solid curves*) and the velocity distribution (*arrows*) at $x = 40H$ are shown. (*a*) Linear stage at $t = 27.8H/C_s$, (*b*) nonlinear expanding stage at $t = 70.0H/C_s$.

netic reconnection at the foot point of magnetic bubbles that are formed. Such twisted flux tubes can also be formed in the nonlinear stage of the magnetic buoyancy instability in a sheared magnetic layer (Cattaneo et al. 1990). When the thickness of the magnetic layer is larger than the scale height, as in model 7, the undular instability dominates over the interchange instability in the nonlinear stage. Thus magnetic loops expand and undulate rather than form isolated flux tubes.

3.6. *Nonlinear Growth of the Three-dimensional Random Perturbation*

Figure 15 shows the evolution of a magnetic layer when random velocity perturbations are imposed inside a horizontal flux sheet (model 8). The maximum value of the perturbation is $0.01C_s$ for V_z. In the linear stage, small wavelength ripples are formed around the interface between the magnetic layer and the gas layer via the interchange instability (Fig. 15*a*). In contrast to the pure interchange case, magnetic loops can rise into the corona in the nonlinear stage (Fig. 15*b*) by precipitating the gas along the magnetic field lines.

Figure 16 shows the surface of constant magnetic field strength ($|B| = 10^{-3}\rho_0^{1/2}C_s$) at $t = 70\tau$. We can see expanding magnetic loops which have the length $\sim 40H \simeq 8000$ km. The width of the magnetic loops increases with time due to horizontal expansion. Further, magnetic field lines are significantly twisted by the vortex motion apparent in Figure 15*b*. The rise speed of the magnetic loops increases with height and the maximum speed at $t = 70.0\tau$ is $2C_s \simeq 20$ km s^{-1}. These results are similar to those in model 1, where the coherent perturbation is imposed.

3.7. *Decelerated Magnetic Loop Formed by an Isolated Magnetic Flux Tube*

If an isolated flux tube has the same temperature as the external medium, it cannot be in magnetostatic equilibrium; it rises buoyantly. Here we study the case in which the unperturbed magnetic flux tube is in magnetostatic equilibrium with the external medium that has the same density distribution. Although this stratification stabilizes the interchange mode, the magnetic flux tube becomes unstable against the undular mode of the magnetic buoyancy instability (see Fig. 9).

Figure 17 shows the nonlinear stage of model 9 ($t = 57.7\tau$). The magnetic loop did not ascend as much as in the sheet model (e.g., model 1), and the rise velocity is smaller ($\simeq 0.3C_s \simeq 3$ km s^{-1}). The evolution of the cross-sectional area of the flux tube is shown in Figure 18. As the top of the loop rises, the magnetic loop expands rapidly in the horizontal direction and occupies the whole volume between $5H \leq z \leq 10H$.

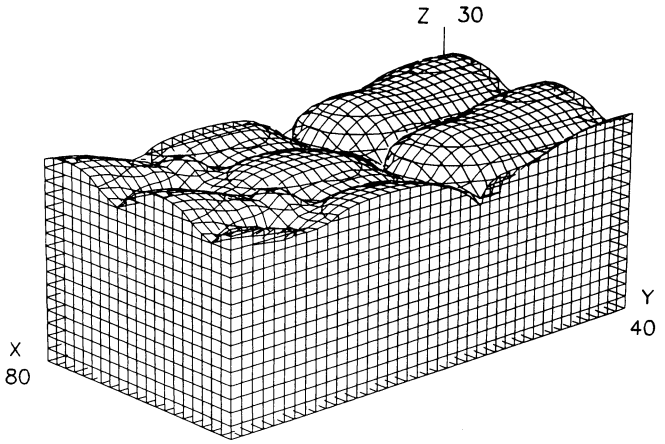

FIG. 16.—Surface of constant magnetic field strength ($|B| = 10^{-3}\rho_0^{1/2}C_s$) in the nonlinear stage ($t = 70.0H/C_s$) of model 8. Twice the computational domain in y-direction is shown by using the periodic boundary condition.

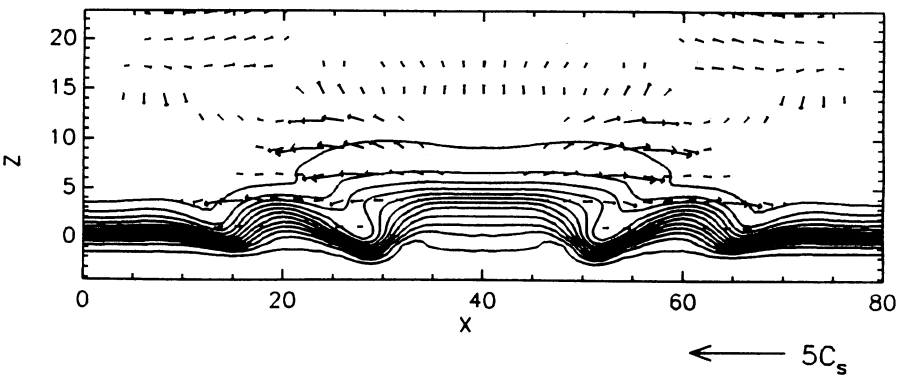

FIG. 17.—Nonlinear, saturated stage ($t = 57.7H/C_s$) of the magnetic buoyancy instability in model 9 ($\beta_0 = 1$, $W = 4H$, $\lambda_x = 20H$) at $y = 20H$. Solid curves show the isocontours of magnetic vector potential (A_y). The arrows show velocity vectors.

The time sequence of the distribution of B_x, V_A/C_s, and V_z/C_s are shown in Figure 19. Although V_z increases with height, it saturates before the loop enters into the corona and V_A stays nearly constant in time, while the horizontal magnetic field and the density decrease exponentially with height. The expansion of the magnetic loop is decelerated after $t = 35.7\tau$ due to the rapid decrease of the magnetic energy density. Since the magnetic pressure term on the right-hand side of equation (13) scales as z^{-1}, it cannot balance the gravity term, which was comparable to the magnetic pressure term in the initial stage. Thus the right-hand side of equation (13) becomes negative and the buoyant motion of the loop is decelerated. The maximum height of the loop is about $12H \simeq 2400$ km.

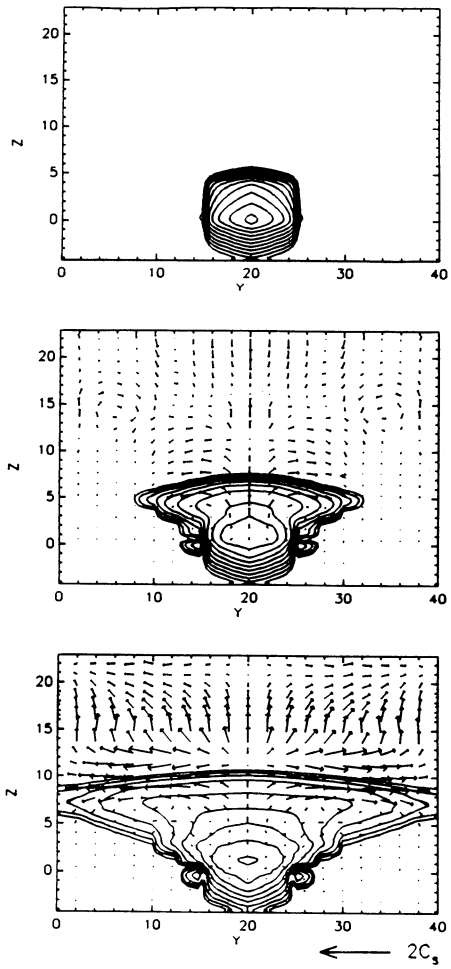

FIG. 18.—Evolution of the cross-sectional area of isolated magnetic flux tube in model 9 at the midpoint of the loop. Solid curves represent the isocontours of B_x. The step width between each curve is taken logarithmic. Arrows show velocity vectors. The unit of velocity vectors is shown in the right bottom. *Top*: $t/\tau = 0.0$. *Middle*: $t/\tau = 35.7$. *Bottom*: $t/\tau = 57.7$.

3.8. *Emergence of Flux Tube Bundles*

In the emerging flux regions (EFRs) of the Sun, magnetic flux appears as bundles of flux tubes (e.g., Zwaan 1987). Figure 20 shows a nonlinear evolution of such bundles (model 10). In this model each flux tube occupies one third of the volume between $Z = 0$ and $Z = 4H$. Four times of the size of the original computational domain is shown in Figure 20 with the periodic boundary condition in the y-direction. Figure 21 shows surface of constant magnetic field strength ($|B| = 10^{-3}\rho_0^{1/2}C_s$) at $t = 43.2\tau$.

After the flux tubes begin to rise, they expand both in the z- and y-directions. The adjacent flux tubes begin to interact with each other at $t = 25.1\tau$. After this stage the expansion becomes nearly one-dimensional in the z-direction. Figure 22 shows that dense rising filaments are formed between adjacent expanding loops. The width of the filaments is $\simeq 4H \simeq 800$ km, and the rise speed is about $C_s \simeq 10$ km s^{-1}. The isodensity surface in Figure 23 also shows such arch filaments. The length of the arch filament is $\simeq 40H \simeq 8000$ km.

The time evolution of the rise speed in Figure 24 is similar to that of the isolated tube (model 9) in the early stage, but the loops are accelerated after $t = 31.0\tau$ when the adjacent expanding loops begin to interact with each other. Also, the time evolution of V_A shows this transition from the isolated 2D tubelike expansion to the collimated 1D sheetlike expansion.

4. SUMMARY AND DISCUSSION

4.1. *Two Regimes of Magnetic Loop Expansion*

We have studied 3D nonlinear evolution of the magnetic buoyancy instability in solar emerging magnetic flux regions. The nonlinear evolution of the magnetic loops can be classified into two regimes; a free expansion and a collimated expansion. The free expansion means an expansion not only in the $x - z$ plane but also allowed in the y-direction in our geometry. On the other hand, we use the term "collimated expansion" for an expansion in the $x - z$ plane but which is restricted in the

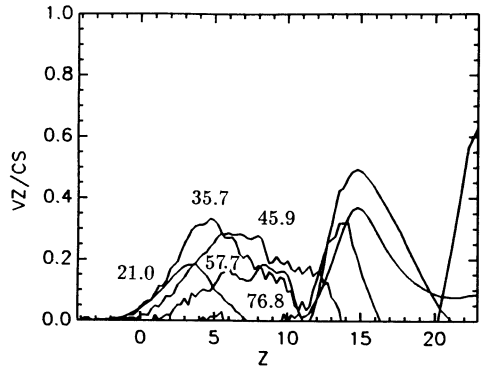

FIG. 19*a*

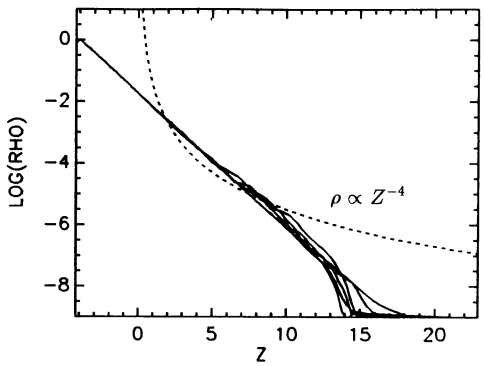

FIG. 19*b*

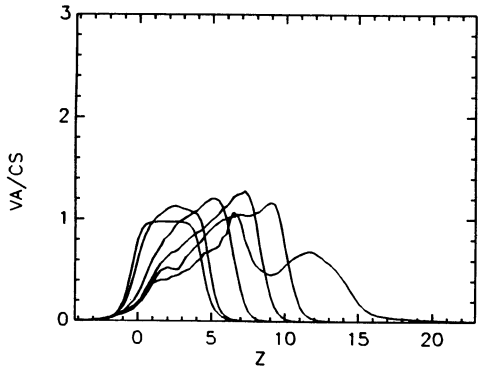

FIG. 19*c*

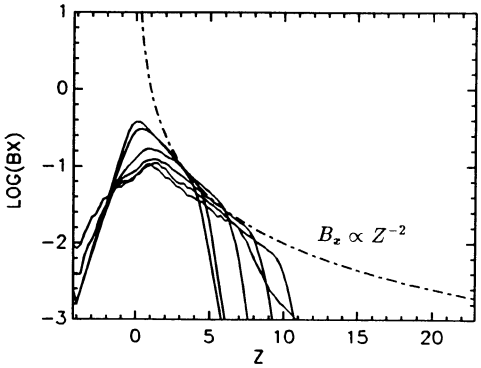

FIG. 19*d*

FIG. 19.—(*a–d*) The same as Fig. 8 but for model 9. The time for each curve is $t/\tau = 0$, 21.0, 35.7, 45.9, 57.7, and 76.8 from left to right. The dashed curve shows z^{-4} dependence for density. The dash-dotted curve shows z^{-2} dependence for B_x.

y-direction due to the close packing of a bundle of magnetic loops in that direction. The free expansion regime appears when the expanding magnetic loop does not interact with other magnetic loops. The cross-sectional area of the loop in this regime increases as z^2 or faster, and the horizontal magnetic field decreases as $B_x \propto z^{-2}$ or faster. The increase in rise speed of the loop saturates shortly after it reaches about half the sound speed and decelerates. The Alfvén speed remains nearly constant in this regime.

In the collimated expansion regime, the magnetic loops expand in a quasi self-similar fashion and the rise speed of the loop increases with height. This regime appears when the magnetic loops are formed from a flux sheet or closely packed bundles of flux tubes. The time evolution in this regime can be fitted to a particular self-similar solution of magnetic loop expansion previously found for 2D loops (Shibata et al. 1989a; Shibata et al. 1990b), where $B_x \propto z^{-1}$, and $\rho \propto z^{-4}$, although for 3D loops the horizontal magnetic field (B_x) decreases slightly faster than z^{-1} due to the horizontal expansion. The rise speed of the loop increases as $V_z/C_s \propto az/H$, where a turns out to be half the linear growth rate of the magnetic buoyancy instability. The speed of the downflow from such expanding loops exceeds the sound and the Alfvén speeds and strong MHD shock waves are created around the footpoints of the magnetic loops.

4.2. *Fundamental Difference between the Interchange and Undular Instabilities in the Nonlinear Stage*

In the nonlinear stage of the pure interchange instability ($k_x = 0$), the expansion of the magnetic loop slows down because $B_x \propto z^{-2}$ and $\rho \propto z^{-2}$, and thus the magnetic pressure force that drives the instability decreases rapidly as $B_x^2/(\rho z) \propto z^{-3}$. That the nonlinear instability of the interchange mode does not exist is in sharp contrast to the undular mode. Thus we conclude that the undulation of the magnetic field lines and the resulting downflow along the loop are of essential importance to sustain the magnetic buoyancy instability continually in the nonlinear stage. Although the linear growth rate of the pure interchange mode ($k_x = 0$) is larger than that of the undular mode, once the rising loops are formed, the undular mode eventually dominates. The overall nature of the magnetic flux expansion is characterized by the properties of the undular mode.

4.3. *Three-dimensional Structure of Magnetic Loops*

When nonsinusoidal perturbations are imposed on a horizontal flux sheet, a highly interleaved structure of magnetic field lines emerges. The wavelength of the imposed perturbation determines the horizontal width of each magnetic loop. If the perturbation is random, interchange mode produces a fine fiber flux structure perpendicular to the magnetic field direction. Later the width of magnetic loops increases with height because of the horizontal expansion.

When the magnetic shear is present, however, the interchange modes for short wavelength modes are stabilized and the width of forming magnetic loops is governed by the most unstable wavelength of the undular mode (Hanawa, Matsumoto, & Shibata 1992). We plan to study the details of the nonlinear evolution of the magnetic buoyancy instability in sheared magnetic fields in a future paper.

In the linear stage of magnetic loop expansion, the adjacent magnetic flux tubes can move almost independently. In the

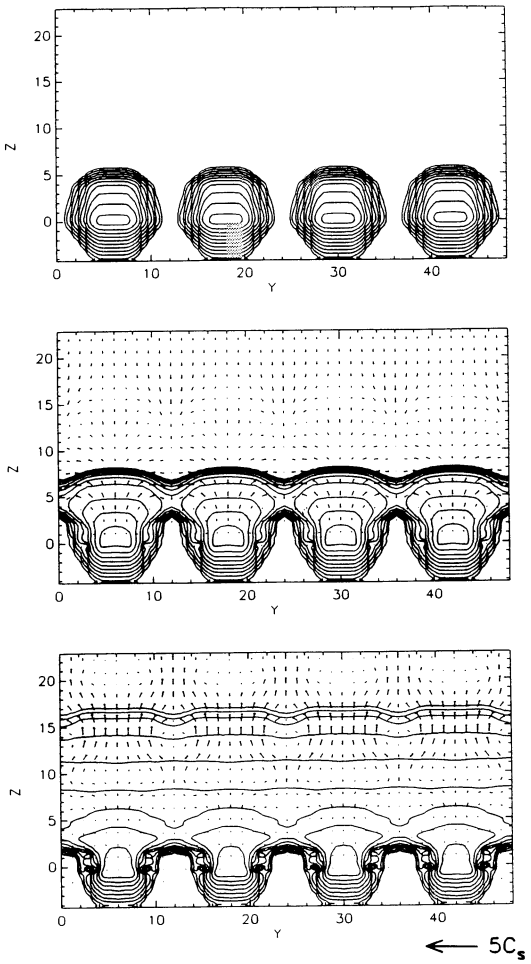

FIG. 20.—Evolution of the cross-sectional area of magnetic loops for model 10 ($\beta_0 = 1$, $W = 4H$, $\lambda_x = 20H$) at $x = 40H$. Four times of the computational area is shown by using the periodic boundary condition. The solid curves show isocontours of B_x. The arrows show velocity fields. The unit of velocity vectors is shown at the right bottom. *Top*: $t/\tau = 0.0$. *Middle*: $t/\tau = 25.1$. *Bottom*: $t/\tau = 43.2$.

nonlinear stage, however, the adjacent magnetic flux tubes interact with each other and collimate tubes against expansion in the horizontal direction. At this stage magnetic flux tubes merge into a bundle of expanding magnetic loops.

Three-dimensional distribution of the density shows a filamentary structure that was previously found for 3D Parker instability in galactic gas disks (Matsumoto & Shibata 1992). Dense filaments are formed in the region between two expanding magnetic loops, where the gas is pinched by the expanding loops.

4.4. *Comparison with Observations*

Here we compare numerical results with some observational data of emerging flux regions (EFRs) on the Sun.

The rise velocity of magnetic loops and filaments obtained from our numerical simulations is comparable to the observed rise velocity (10–15 km s^{-1}) of arch filaments (Bruzek 1967, 1969; Chou & Zirin 1988) when the loops are created from a magnetic flux sheet or the initial magnetic flux is confined as bundle of flux tubes. When the initial flux is confined in an isolated magnetic flux tube, however, the maximum rise speed

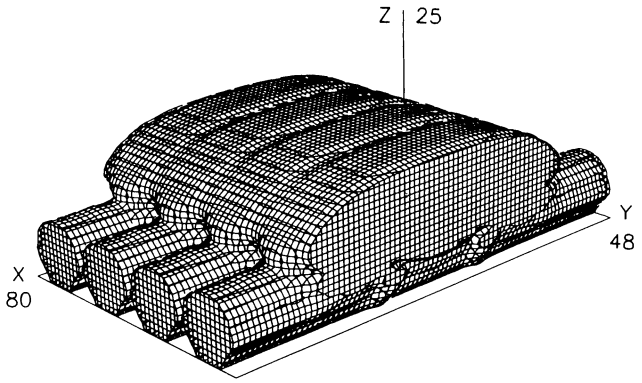

FIG. 21.—The surface of constant magnetic field strength ($|B| = 10^{-3}\rho_0^{1/2}C_s$) in model 10 ($t = 43.2\tau$). Four times of the computational domain in y-direction is shown by using the periodic boundary condition.

($V_z \simeq 4$ km s^{-1}) appears to be too small to explain the observed rise velocity of arch filaments.

The length of the rising loop in our numerical simulation is about the wavelength of the most unstable undular mode ($\simeq 20H = 4000$ km) in the photosphere. The length increases with height up to $\simeq 10^4$ km at $z \simeq 5000$ km, and further increases in the corona. These results are consistent with the

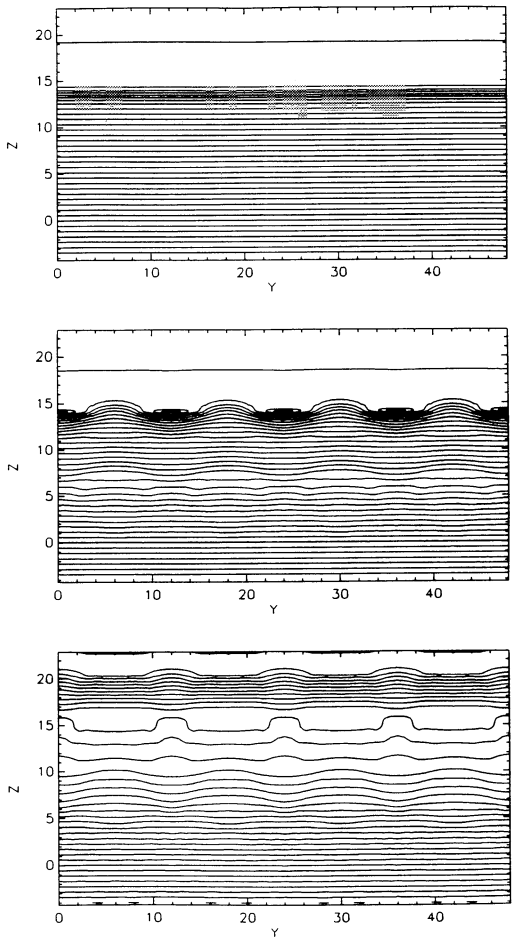

FIG. 22.—Rising motion of dense filaments in model 10. Solid curves show isocontours of the density at $x = 40H$. The step width of the contour curves is 0.25 in logarithmic scale. *Top*: $t/\tau = 0.0$. *Middle*: $t/\tau = 25.1$. *Bottom*: $t/\tau = 43.2$.

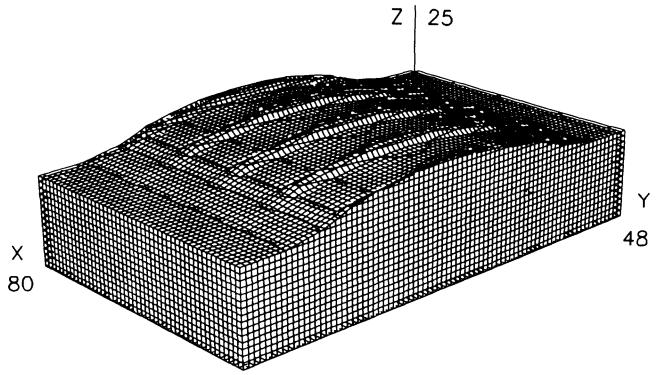

FIG. 23.—Density isocontour surface ($\rho/\rho_0 = 6.0 \times 10^{-7}$) in the collimated expansion stage ($t = 43.2H/C_s$) of model 10.

observed separation of two polarities (3000–20,000 km), and the dimension of arch filaments ($\simeq 10^4$ km).

The downdraft speed found in simulations is about $3C_s$–$5C_s$ = 30–50 km s^{-1} in our models. Strong shock waves are formed near the footpoints of magnetic loops. These shock waves and the associated heating of the chromosphere may be the origin of bright plages observed near arch filament systems (Bumba & Howard 1965; Born 1974; Shibata et al. 1989b).

The magnetic flux initially stored in the horizontal magnetic flux sheet in our numerical model is 10^{20} Mx, when the width and thickness of the flux sheet are $40H$ and $4H$, respectively. The observed magnetic flux in solar active regions ranges from 10^{22} Mx in large active regions to 10^{18} Mx in ephemeral regions (Zwaan 1987). It is known that there is a threshold flux 0.5×10^{20}–1.0×10^{20} Mx (Chou & Wang 1987) for an arch filament formation. In our numerical models, expanding magnetic loops are formed when the magnetic flux is greater than 0.3×10^{20} Mx (model 10). When the magnetic flux is 10^{19} Mx (model 9), magnetic loops cannot expand into the corona. The latter may correspond to ephemeral regions.

Recently, the Soft X-ray Telescope (SXT) on the *Yohkoh* mission (Tsuneta et al. 1991) enabled us to observe the evolution of EFRs in coronal X-rays with high spatial and temporal resolution. Comparing the Hα images with soft X-ray images, it is found that soft X-ray bright features coincide well in space with Hα arch filament systems in EFRs (Kawai et al. 1992, 1993). Soft X-ray images show looplike structure in EFRs (Kawai et al. 1992, 1993), which supports the idea that cool magnetic loops ($T \simeq 10^4$ K) in the photosphere evolve into X-ray–emitting coronal loops ($T \simeq 10^6$ K) by some heating mechanisms. Numerically observed magnetic loops in the coronal region may correspond to the soft X-ray loops if proper heating mechanisms are included.

The soft X-ray images of EFRs show that the length of soft X-ray loops increases with time. The expansion speed of soft X-ray loops is 2–5 km s^{-1} in the early stage of EFRs (a few hours after their birth), and their length increases up to 4–6 $\times 10^4$ km (Ishido et al. 1993). In a typical numerical model (model 1), the horizontal expansion speed of magnetic loops is 7–10 km s^{-1} just after their emergence into the corona. This slightly faster speed is not inconsistent with observation because the numerical simulation covers only very early stage

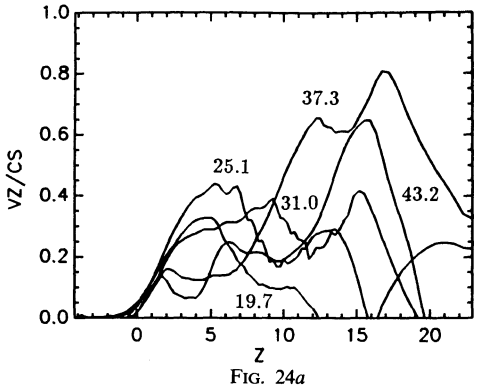

FIG. 24a

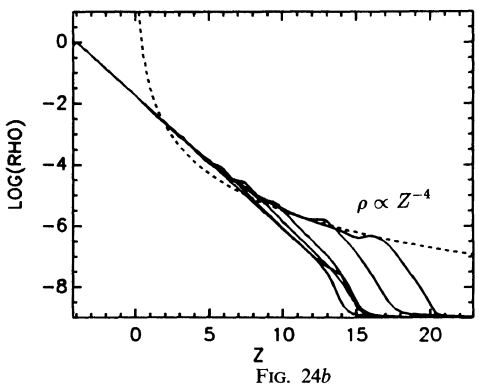

FIG. 24b

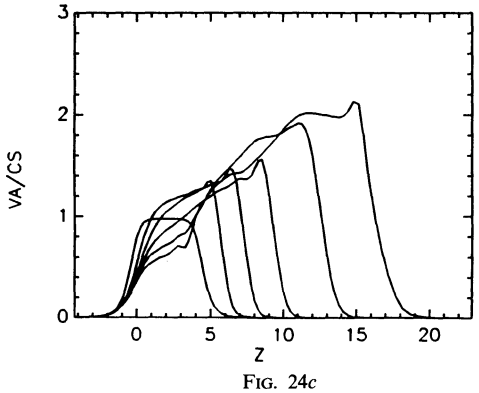

FIG. 24c

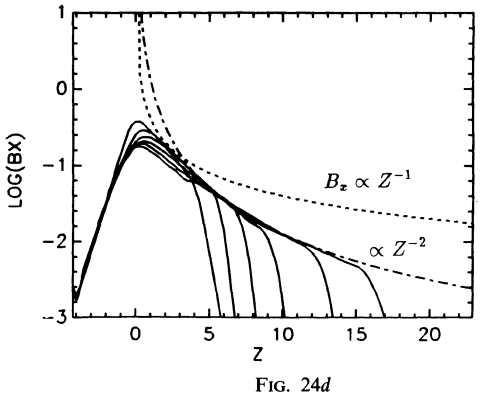

FIG. 24d

FIG. 24.—(*a*–*d*) The same as Fig. 8 but for model 10. The dashed curves show z^{-4} and z^{-1} dependence for density and B_x, respectively. The dash-dotted curve shows z^{-2} dependence. The time is t/τ = 0, 19.7, 25.1, 31.0, 37.3, and 43.2, from left to right.

of magnetic flux expansion into the corona (15 minutes after the magnetic flux emerged into the photosphere).

A coordinated observation between *Yohkoh* and ground-based observatories indicates that the soft X-ray loops cover a wider area than Hα arch filaments, and that the width of soft X-ray loops is thicker than Hα arch filaments (Kawai et al. 1993). These features are consistent with numerical results. Numerical results also predict that (1) when the sub-photospheric magnetic field is not sheared, the soft X-ray loops are parallel to the Hα arch filaments, (2) soft X-ray loops cover the area between two Hα filaments, and (3) soft X-ray loops are twisted by vortex motion generated by horizontal expansion.

We are currently correlating our 3D MHD simulation efforts with the *Yohkoh* observations. The details of this comparative study will appear in subsequent papers.

In conclusion, our numerical results corroborate the observed signatures ranging from the total magnetic flux to the various morphologies of solar active regions. These morphological signatures include the presence of looplike arch filament systems for active regions, shocks near the foot region of the arch, isolated flux tube dynamics for the ephemeral region, and the spatial relation between the Hα filaments and soft X-ray loops.

The authors thank L. Acton, K. Strong, S. Tsuneta, T. Shimizu, N. Nitta, G. Kawai, H. Kurokawa, M. Akioka, Y. Ishido, and other members of Yohkoh SXT team for supplying us with the results of their observation. The discussions with Y. Uchida, W. Horton, R. Rosner, H. Spruit, T. Hanawa, A. McAllister, Y. Suematsu, and Y. Todo were helpful for completion of this work. We also acknowledge M. J. LeBrun and G. Furnish for the implementation of PLPLOT plotting library, and G. Tarkenton for carefully reading the manuscript. Numerical computations were performed on the Cray Y-MP8/864 at the Center for High Performance Computation of the University of Texas system, FACOM VP200 at the National Institute of Fusion Science of Japan, and NEC SX-2A at the Institute of Supercomputing Research, Recruit, Co. Ltd. This work is supported in part by the NSF ATM-91-13576, NASA PR1058109, and a Grant-in-Aid for Scientific Research by the Ministry of Education, Science and Culture (03302013).

REFERENCES

Acheson, D. J. 1979, Sol. Phys., 62, 23
Born, R. 1974, Sol. Phys., 38, 127
Bruzek, A. 1967, Sol. Phys., 2, 451
———. 1969, Sol. Phys., 8, 29
Bumba, J., & Howard, R. 1965, ApJ, 141, 1492
Cattaneo, F., Chiueh, T., & Hughes, D. W. 1990, J. Fluid Mech., 219, 1
Cattaneo, F., & Hughes, D. W. 1988, J. Fluid Mech., 196, 323
Chou, D., & Wang, H. 1987, Sol. Phys., 110, 81
Chou, D., & Zirin, H. 1988, ApJ, 333, 420
Hanawa, T., Matsumoto, R., & Shibata, K. 1992, ApJ, 393, L71
Horiuchi, T., Matsumoto, R., Hanawa, T., & Shibata, K. 1988, PASJ, 40, 147
Hughes, D. W. 1985, Geophys. Astrophys. Fluid Dynamics, 32, 273
Ishido, Y., et al. 1993, in preparation
Kaisig, M., Tajima, T., Shibata, K., Nozawa, S., & Matsumoto, R. 1990, ApJ, 358, 698
Kawai, G., Kurokawa, H., Tsuneta, S., Shimizu, T., Shibata, K., Acton, L., Strong, K., & Nitta, N. 1992, PASJ, 44, L193
Kawai, et al. 1993, in preparation
Matsumoto, R., Horiuchi, T., Shibata, K., & Hanawa, T. 1988, PASJ, 40, 171
Matsumoto, R., & Shibata, K. 1992, PASJ, 44, 167
Nozawa, S., Shibata, K., Matsumoto, R., Sterling, A. C., Tajima, T., Uchida, Y., Ferrari, A., & Rosner, R. 1992, ApJS, 78, 267
Parker, E. N. 1966, ApJ, 145, 811
———. 1979, in Cosmological Magnetic Fields (Oxford Univ. Press), p. 314
Richtmyer, R. D., & Morton, K. W. 1967, in Difference Methods for Initial-Value Problems, 2nd ed. (New York: Interscience), 365
Rubin, E. L., & Burstein, S. Z. 1967, J. Comp. Phys., 2, 178
Shibata, K. 1983, PASJ, 35, 263
Shibata, K., Nozawa, S., Matsumoto, R., Sterling, A. C., & Tajima, T. 1990a, ApJ, 351, L25
Shibata, K., Tajima, T., & Matsumoto, R. 1990b, Phys. Fluids, B2, 1989
Shibata, K., Tajima, T., Matsumoto, R., Horiuchi, T., Hanawa, T., Rosner, R., & Uchida, Y. 1989a, ApJ, 338, 471
Shibata, K., Tajima, T., Steinolfson, R. S., & Matsumoto, R. 1989b, ApJ, 345, 584
Shibata, K., & Uchida, Y. 1985, PASJ, 37, 31
Tsuneta, S., et al. 1991, Sol. Phys., 136, 37
Umemura, S., Iki, K., Shibata, K., & Sofue, Y. 1988, PASJ, 40, 25
Zirin, H. 1970, Sol. Phys., 14, 328
———. 1972, Sol. Phys., 22, 34
Zwaan, C. 1987, ARA&A, 25, 83